Materials Science and Engineering B 288 (2023) 116163

Contents lists available at ScienceDirect

Materials Science & Engineering B

journal homepage: www.elsevier.com/locate/mseb

A sensitive enzyme-free electrochemical sensor composed of Co_3O_4/CuO@MWCNTs nanocomposites for detection of L-lactic acid in sweat solutions

Bairui Tao [a,*,1], Wenbo Yang [a,1], Fengjuan Miao [a,*], Yu Zang [b], Paul K. Chu [c]

[a] College of Communications and Electronics Engineering, Qiqihar University, Heilongjiang 161006, China
[b] College of Materials Science and Engineering, Qiqihar University, Wenhua street 42, Qiqihar, China
[c] Department of Physics, Department of Materials Sciences and Engineering, and Department of Biomedical Engineering, City University of Hong Kong, Tat Chee Avenue, Kowloon, Hong Kong, China

ARTICLE INFO

Keywords:
L-Lactic acid
Non-enzymatic detection
Electrochemical sensor
Nanocomposites
Nickel foam

ABSTRACT

L-Lactate acid (L-LA) is an important organic biomolecule and exists in human sweat thus making direct detection by current techniques challenging. It is thus important to develop a non-enzymatic L-LA sensor with high sensitivity and low cost. Herein, multidimensional mutli-walled carbon nanotube nanocomposites (Co_3O_4/CuO@MWCNTs NCs) incorporated with copper and cobalt oxide are prepared on nickel foam (NF, Surface area = 1 cm^2) hydrothermally for L-LA detection. The Co_3O_4/CuO@MWCNTs NCs are analyzed by powder X-ray diffraction (XRD), field-emission scanning electron microscopy (FE-SEM), transmission electron microscopy (TEM), X-ray photoelectron spectroscopy (XPS), and Ultraviolet–visiblespectroscopy (UV–VIS). Experimental results show that as an enzyme-free L-LA sensor, the Co_3O_4/CuO@MWCNTs NCs constitute a simple and low-cost detector to monitor L-LA in human sweat and the materials which yield high sensitivity and selectivity have broad prospects in the medical and health fields.

1. Introduction

L-LA is one of the potential biomarkers to assess human conditions in clinical medicine or sports because the L-LA level in human blood is closely related to oxygenation of human tissues [1]. Reliable L-LA detection is particularly critical in emergency situations such as bleeding, hypoxia, respiratory failure, and sepsis and moreover, L-LA monitoring benefits athletes by monitoring the muscle activity to prevent injury arising from excessive muscle use or fatigue [2]. The normal L-LA concentration range is between 0.3 and 1.3 mM and concentrations of L-LA in blood exceeding 5 mM may lead to lactic acidosis [3]. In clinical medicine, hyperlactic acidemia is an index of systemic tissue hypoxia and it has been shown that L-LA is related to the production of cancer cells in organs and tissues. Persisting lactic acidosis may affect liver metabolism if L-LA production exceeds the metabolic rate that can be sustained by the liver [4]. It has also been observed that high levels of lactic acid in tumor cells in the head, neck and uterus may produce a higher risk of cancer metastasis and therefore, accurate measurement of L-LA can provide important information to discern metastatic and benign tumors in these areas [5,6,29].

Clinical detection of L-LA can be carried out by several methods such as chemical oxidization of L-LA, indirect spectrophotometry, chromatography, magnetic spectroscopy, enzyme kits or biosensors [7,8], but they tend to have drawbacks such as the large size, heavy weight, lack of mechanical flexibility, complex operation, requirement for trained medical staff, instability, and high cost [9,10]. Compared to these methods, non-enzymatic electrochemical lactic acid sensors have advantages such as the simple structure, portability, selectivity, and user-friendliness. Non-enzymatic lactate sensors use a variety of nanostructured materials. G Rattu and et al., have reported a ZnO nanocomposite (ZnO NPs) optical sensor for L-LA detection and got a low detection limit of 3.98 mM[11], YH Nien and et al., have reported a way of biosensor based on copper doped zinc oxide (CZO) films and got a sensitivity of 25.32 mV/mM[12], Arivazhagan M and Maduraiveeran G are reported an ultrafine nanocluster of nickel-sulfieds (NiS-NC@NiS-MS) with a low detection limit of 0.5 μM[13], Maduraiveeran G and

* Corresponding authors.
E-mail addresses: tbr_sir@163.com (B. Tao), miaofengjuan@163.com (F. Miao).
[1] Bairui Tao and Wenbo Yang are co-first authors.

https://doi.org/10.1016/j.mseb.2022.116163
Received 13 October 2022; Received in revised form 16 November 2022; Accepted 17 November 2022
Available online 7 December 2022

Chen A are reported an enzyme-mimicking electrochemical NiO@Au nanocomposite to detection lactic acid and got a low detection limit of 11.6 μM[14]. In contrast, enzyme-free electrochemical sensors have strong advantages, also, Metal oxide nanoparticles are of a great interest in electrochemical applications and have been used to decorate carbon nanotubes-based materials. Well-aligned, multi-walled carbon nanotubes (MWCNTs) are novel sensing materials on account of the high electrical conductivity, large length-diameter ratio, large surface area, and excellent mechanical strength [15–17,47]. MWCNTs also show good dispersion in water and low cytotoxicity and can easily be loaded with other nanomaterials or biomolecules [18–20,36–39]. Rational selection of matrix can make negative dielectric materials have multifunctional applications, such as high mechanical strength, flexibility, chemical stability, light absorption performance, and so on. The precondition of negative dielectric property is the formation of conductive network consisting of nano- or micro- conductive particles, so the composition of fillers shows difference in adjusting the negative dielectric constant; the fillers can be metal, carbon, conductive ceramics, and conductive polymer. The negative permittivity can be achieved by constructing percolation conducting network of metals or carbon (such as Fe, Co, Ni, Ag, CNTs, and GR) in insulation matrix, therefore, we choose cobalt oxide and carbon nanotubes combined to increase the conductivity of the electrode and light absorption performance and its flexibility. The coordination of carbon nanotubes on the porous nickel foam electrode can effectively reduce the dielectric constant and material density, thus making the nanocomposite electrode lighter[44–46].

In thiswork, a novel, lightweight, and highly sensitive non-enzymatic composite made of multi-walled carbon nanotubes decorated with copper oxide and cobalt oxide on NF is prepared by a hydrothermal method and annealing. The L-LA sensing properties are assessed in simulated human sweat for the first time and the advantages of the fabrication method includes simple preparation and easy control of the reaction temperature and conditions.

2. Experimental section

2.1. Reagents and solutions

L-LA, uric acid, ascorbic acid, maltose, lactose, sucrose, chitosan, oxalic acid dehydrate, folic acid, dipotassium phosphate (K_2HPO_4), and monopotassium (KH_2PO_4) were obtained from Macklin and sodium hydroxide (NaOH), Copper sulfate ($CuSO_4{\cdot}5H_2O$), MWCNTs, cobalt nitrate hexahydrate ($Co(NO_3)_2{\cdot}6H_2O$), sodium chloride (NaCl), hydrated ammonia ($NH_3{\cdot}H_2O$), and urea (CH_4N_2O) were purchased from Shanghai Hans Chemical Industry Co. Ltd. Nickel foam was purchased from Changsha Lyrun New Materials Corporation. All the reagents were analytical grade and used without additional purification. Deionized water (DD) was used in the preparation of all the solutions and all the experiments were conducted at room temperature unless stated otherwise.

2.2. Hydrothermal synthesis of CuO@MWCNTs NCs

The nickel foam was cut into square samples with an area of 1 cm × 1 cm, cleaned ultrasonically with DD, HCl, and ethanol for 15 min each to remove impurities and enhance the conductivity of NiO, and dried at 60 °C for half an hour. The copper oxide and cobalt oxide nanocomposites were prepared with copper sulfate, multi-walled carbon nanotubes, cobalt nitrate, urea and sodium hydroxide as precursors by a simple and fast hydrothermal technique. $CuSO_4{\cdot}5H_2O$ (2.5 g) and MWCNTs (0.25 μg) were dissolved in 50 mL of distilled water and cleaned ultrasonically for one hour. NaOH was added to adjust the pH to 10 and the solution was stirred magnetically at 90 °C for 6 h. The solution and NF were placed in a 50 mL Teflon-lined stainless steel autoclave, sealed, and heated to 120 °C for 22 h. After cooling to room temperature naturally, the product was taken out and rinsed with DD several times. By hydrothermal process, the solution produces some chemical reaction in the teflon autoclave, which causes CuO@MWCNTs to deposit on the nickel foam. The chemical reactions are follows:

$$NaOH \rightarrow Na^{+}+OH^{-} \quad (1)$$

$$CuSO_4 \rightarrow Cu^{2+}+SO_4^{2-} \quad (2)$$

$$Na^{+}+OH^{-}+Cu^{2+}+SO_4^{2-}\rightarrow Cu(OH)_{2(aq)} + Na_2SO_{4(s)}\downarrow \quad (3)$$

$$Cu(OH)_{2(aq)} + MWCNT_{(Dispersed)} \rightarrow CuO@MWCNT_{(s)}\downarrow+H_2O \quad (4)$$

2.3. Hydrothermal synthesis of Co_3O_4/Cuo@MWCNTs NCs

The Co_3O_4/Cuo@MWCNTs NCs were synthesized by a secondary hydrothermal method. Co $(NO_3)_2$ $6H_2O$ (0.218 g) and CH_4N_2O (0.225 g) were dissolved in 50 mL of DD with stirred vigorously for 5 min to form a homogeneous solution. It was placed in a 50 mL Teflon-lined stainless steel autoclave together with the nickel foam and maintained at 130 °C for 8 h. Afterwards, the product was dried at 60 °C for 30 min, annealed at 500 °C for 4 h, and cooled to room temperature. The process is illustrated in Fig. 1.

2.4. Preparation of sweat

g of CH_4N_2O, 5 g of NaCl, and 940 μL of L-LA were placed in 1000 mL of deionized water and stirred to form a uniform solution. The pH was adjusted to 6.5 with $NH_3{\cdot}H_2O$ and used within within 3 h[49].

2.5. Materials characterization

The Co_3O_4/CuO@MWCNTs NCs were characterized by X-ray diffraction (XRD), high-resolution transmission electron microscopy (FE-TEM), and selected-area electron diffraction (SAED) on the Hitachi H-7650. Elemental mapping was performed on the SEM and X-ray photoelectron spectroscopy (XPS, VG Scientific ESCALAB250) was carried out to analyze the binding energy and chemical composition of the specimens, Ultraviolet–visiblespectroscopy (UV–VIS Lamda35) determines molecular composition and structure.

2.6. Electrochemical evaluation

The electrochemical properties of the sensor were determined using the standard three-electrode system in which the saturated Ag/AgCl electrode, platinum electrode, and nanostructured electrode were the reference, counter. and the working electrodes respectively, Current-voltage (I-V) and cyclic voltammetry (CV) experiments were performed on the CHI 660E (Chenhua Instrument, China) in a test solution of PBS (pH = 8, 0.1 M, 50 mL). CV was conducted in the potential window of 0–0.8 V at scanning rates ranging from 10 to 90 mV/s and the I-V experiments were carried out in the potential window of 0–1.5 V at a scanning rate of 50 mV/s.

2.7. L-LActate sensing protocol and HPLC validation

A reverse-phased (RP) HPLC was used for L-LActate quantification. The isocratic mobile phase was a mixture of acetonitrile/water (5:95). The flow rate was at 1.0 mL/min, and absorbance was monitored at 210 nm by the tunable absorbance detector. Each sample analysis was performed three times. Sensor validation with HPLC was concluded by equation (5):

$$W_m = 1000MW(K^{'}+1)\frac{S}{N}\frac{(N^0)L^{0.5}}{\varepsilon Lcd^2cN^{0.5}} \quad (5)$$

where MW is molecular weight, Wm is minimum weight, ε is molar

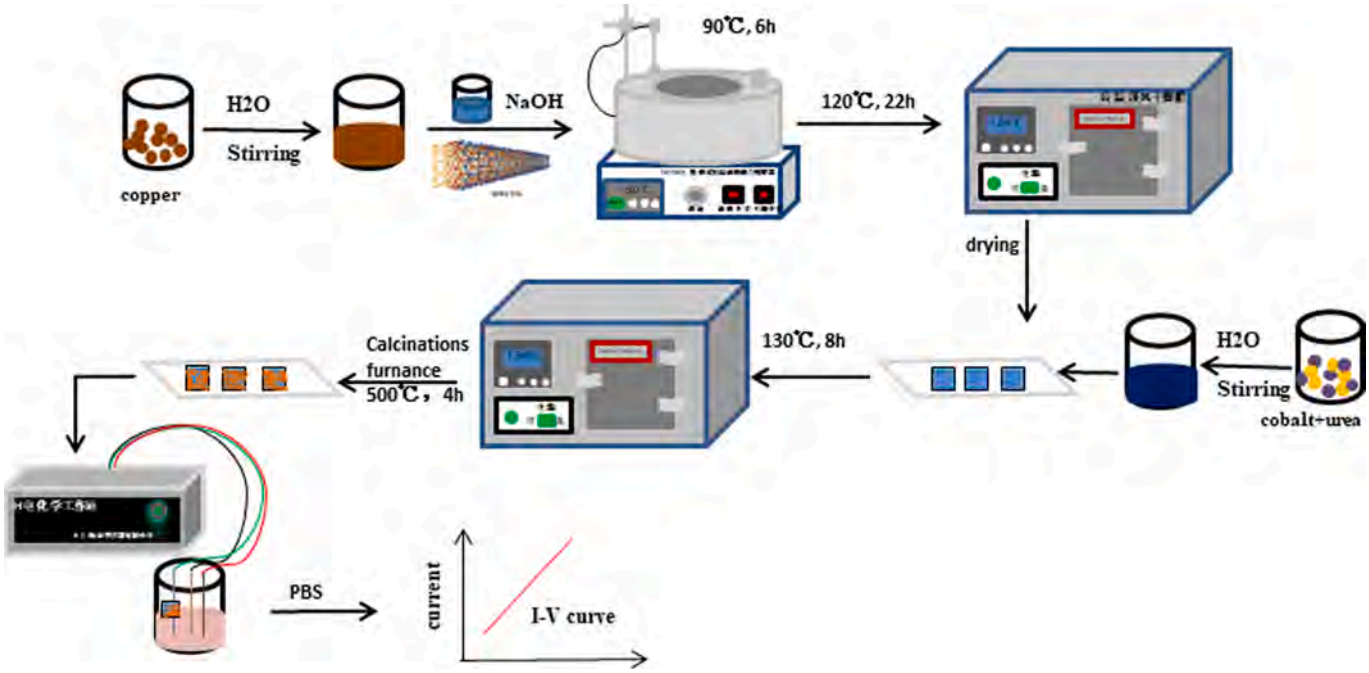

Fig. 1. Preparation of Co_3O_4/Cuo@MWCNTs NCs by the wet chemical technique, electrode modification, and expected current-voltage (I-V) curve for detection of bio-molecules.

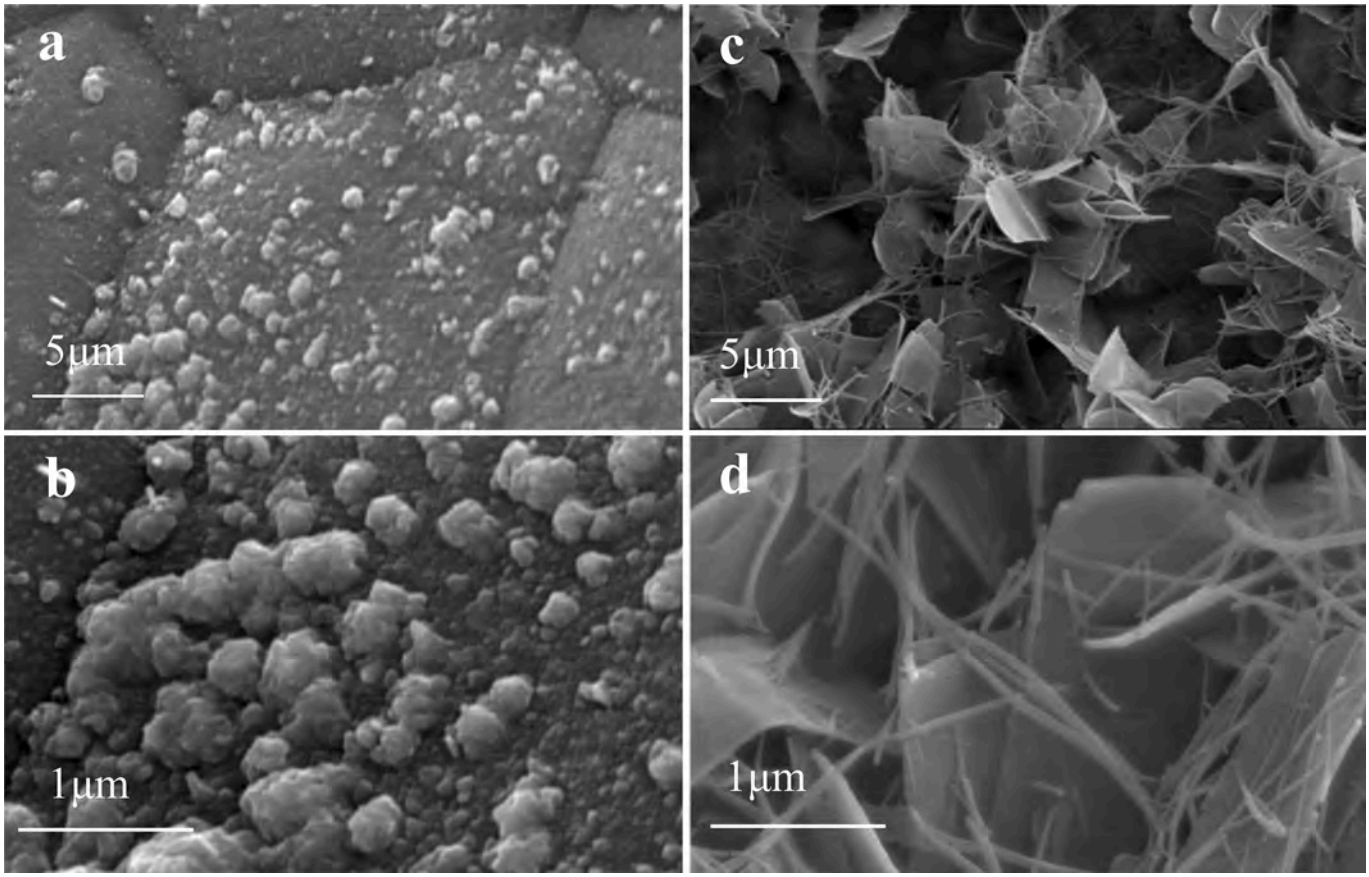

Fig. 2. FE-SEM images: **(a, b)** CuO NPs and **(c, d)** Co_3O_4/Cuo@MWCNTs NCs at different magnifications.

absorptivity, S/N is signal to noise ratio, LC is the detector, d is diameter, L is column length, $K^{'}$ is a capacity factor, N is plate number, and N^{0} is baseline noise.

3. Results and discussion

3.1. Fe-SEM

Fig. 2 shows that morphology at different magnifications is depicted, the aggregated CuO and Co_3O_4 NPs adsorb on the surface of the MWCNTs confirming successful synthesis of Co_3O_4/CuO@MWCNTs NCs. The morphology of the CuO NCs in Fig. 2a and 2b reveal a different magnifications morphology and Fig. 2c and 2d depict the morphology of the Co_3O_4/Cuo@MWCNTs NCs by FE-SEM, also, at a low-magnification and a high-magnification morphology separately. Fig. 2c reveals that the platelet structure is densely organized to form a flower-like structure with a large surface area. Fig. 2d shows that the multi-walled carbon nanotubes are evenly distributed on the nickel foam and provide attachment sites for the spherical CuO particles and Co_3O_4 nanoflowers. Fig. 2c and 2d show that the FE-SEM images of the Co_3O_4/CuO@MWCNTs NCs on NF at different magnifications revealing that the round CuO particles and Co_3O_4 nanoflowers adsorb on the multi-walled carbon nanotubes forming nanoparticles[31–34]. The porous structure facilitates charge transfer in the electrolyte, increases the rate of reaction for ions and electrons, and increases the current. The elemental distribution and composition of the Co_3O_4/CuO@MWCNTs NCs are determined by Mapping as shown in Fig. 3. Fig. 3b-f show that cobalt, copper, carbon, oxygen, and nickel are uniformly distributed and anchor well on the nickel foam.

3.2. TEM and HR-TEM

The Co_3O_4/CuO@MWCNTs NCs are examined by TEM and aggregated round particles are shown in Fig. 4a. The granular of CuO and multi-walled carbon nanotubes have a tubular distribution and Co_3O_4 exhibits the flower-like morphology. The nanocomposite forms a stable and interconnected three-dimensional network consistent with SEM. The HR-TEM images in Fig. 4b disclose lattice fringes with d-spacings of 0.82 nm, 1.27 nm, and 1.13 nm that can be indexed to the (210), (004), and (551) planes of multi-walled carbon nanotubes, copper oxide, and cobalt oxide[35]. The SAED pattern in Fig. 4c shows the polycrystalline structure. Fig. 4d displays that the EDS maps of C, Co, Cu, O, and Ni disclosing uniform coverage of Co_3O_4/CuO@MWCNTs NCs confirming successful synthesis on NF.

3.3. XRD

Fig. 5(a) shows three broad peaks at 44.4, 51.6, and 76.1°corresponding to (111), (200), and (220), respectively (Ni: JCPDS card no. 01-1258) and the other three peaks stem from Co_3O_4, C, and CuO. According to Co_3O_4 (JCPDS card no.43-1003), the peaks at 2θ of 36.9°, 65.2°, and 78.4° correspond to the (311), (440), and (622) and those at 2θ = 43°and 75.3°arise from the (104) and (0120) planes of carbon (JCPDS card no. 50-1085). The peaks at 2θ = 35.2°, 38.5°, and 48.6°are associated with the (002), (202), and (220) planes of CuO (JCPDS card no. 44-0706). Fingerprint characterization and phase percentage determination were performed using XRD patterns. Phase identification was performed using the search-matching program X'Pert HighScore Plus, and then the structure and microstructure parameters of the detected phase were determined using the Rietveld method implanted by the MAUD program, Rietveld adjustments were applied for simultaneous structural and microstructural investigations of the formed phase, According to the distribution of these vacancies and cations amongst the different lattice sites, various crystal symmetries can be adopted which are evidenced in the observed XRD patterns [40,41]. Also, the refined image is shown in Fig. 5(b). The nickel foam substrate can also be detected by XRD and the results verify the presence of copper oxide nanoparticles, cobalt oxide nanoflakes, and carbon nanotubes.

3.4. XPS

XPS deconvolution is a kind of operation. First, it is abstract and symbolic. XPS can provide sample composition, chemical state, surface

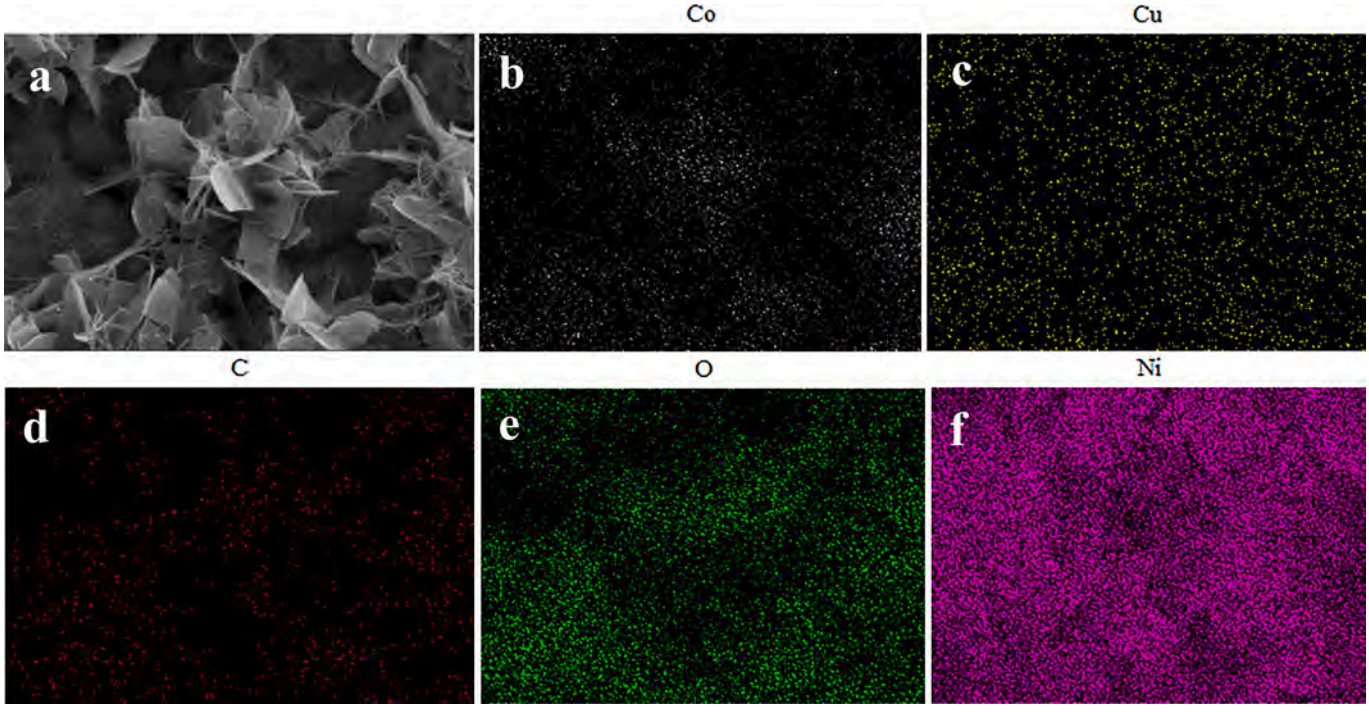

Fig. 3. Mapping of Co_3O_4/Cuo@MWCNTs NCs: **(b)** Co, **(c)** Cu, **(d)** C, **(e)** O, (f) Ni.

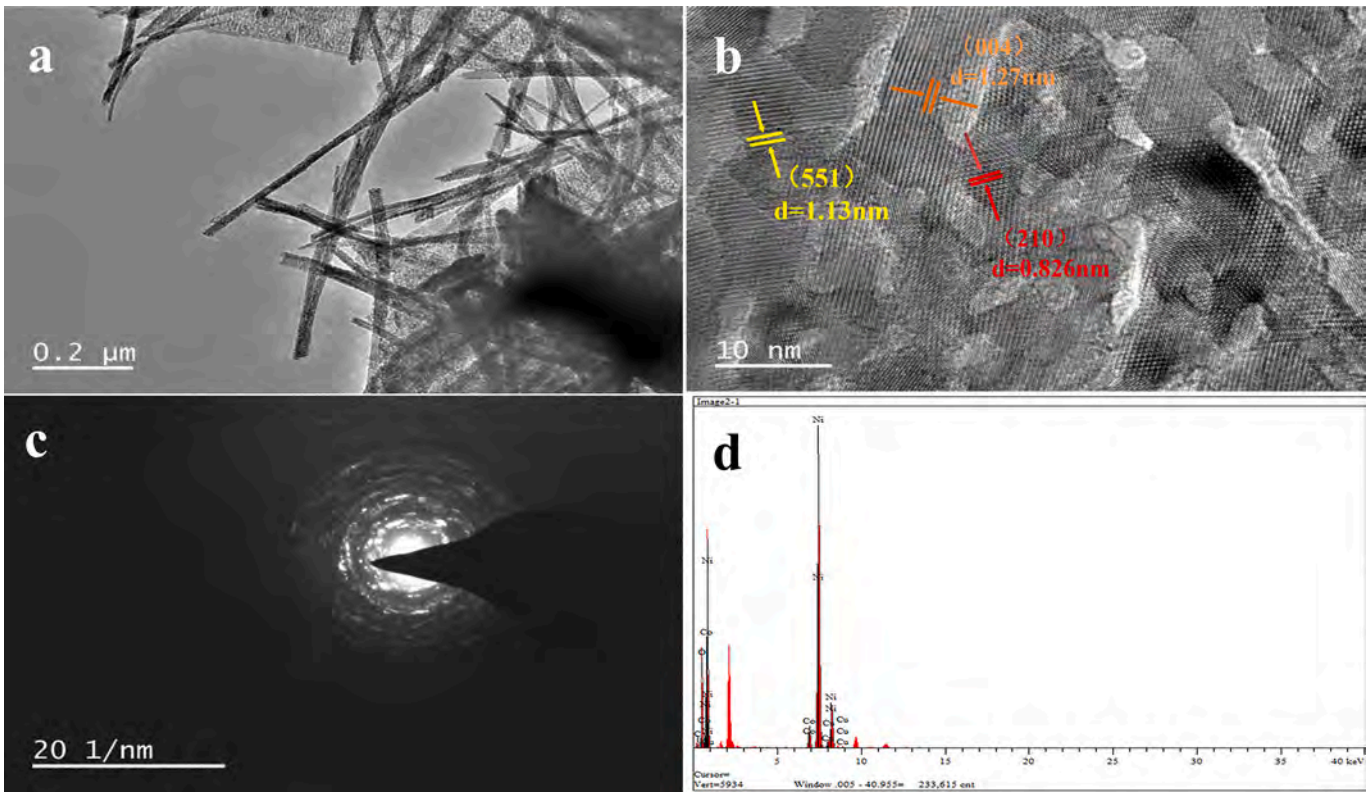

Fig. 4. **(a)** TEM image of Co_3O_4/Cuo@MWCNTs NCs, **(b)** HR-TEM image of Co_3O_4/Cuo@MWCNTs NCs, **(c)** SAED pattern and (**d**) EDS test of the obtained electrode.

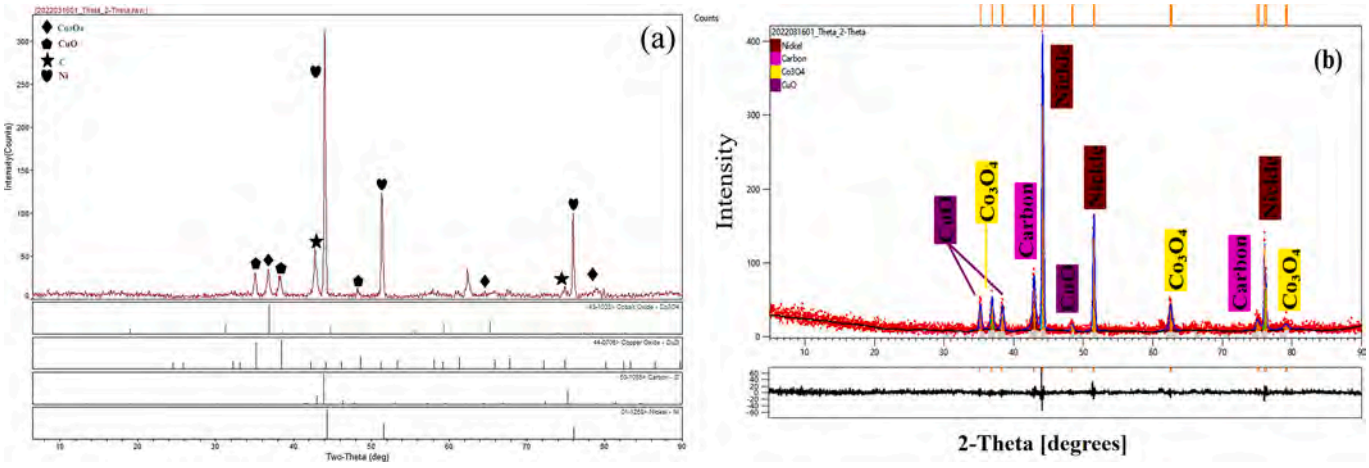

Fig. 5. XRD patterns: **(a)** XRD patternsof the Co_3O_4/Cuo@MWCNTs NCs on NF, **(b)** Rietveld refinement pattern fitting for Co_3O_4/Cuo@MWCNTs NCs samples.

adsorption, surface state, surface valence electron structure, atomic and molecular chemical structure, chemical bonding, etc. In this experiment, because the substrate is nickel foam, there is a strong Ni peak spectrum. The full spectrum of Fig. 6(a) shows the presence of Cu, Ni, Co, O, and C elements. This proves the successful synthesis of nano-complexes in our experimental samples. Single spectral analysis of element peaks is performed, as shown in Fig. 6 (b), (c), (d) and (e). The survey XPS spectrum is presented in Fig. 6(a) and the C 1s spectrum and include C–C bond in Fig. 6(b) shows a peak at 284.2 eV, Atomic is 19.19%[21]. The spin-energy separation between Co $2p_{3/2}$ and Co $2p_{1/2}$ is approximately 15 eV verifying the existence of Co^{2+} and Co^{3+} and two peaks at 779.4 and 795 eV are observed from the Co 2*p* spectrum in Fig. 6(c), the orbital energy difference between Co^{2+} and Co^{3+}(ΔE) are 15.37 eV and 15.46 eV, the atomic is 9.17%.[19]. The Cu 2*p* spectrum in Fig. 6(d) shows one split spin-orbital components ($\Delta_{metal} = 19.75$ eV) and one satellite peak. The peak at 932.7 eV corresponds to the 2 $p_{3/2}$ peak of copper and that at 942.4 eV is associated with the 2 $p_{1/2}$ peak of copper, The peak ratio is comparable to that of nano-CuO reported earlier and it's atomic is 0.42%, corroborating the existence of the Cu^{+}[22]. The O 1*s* spectrum in Fig. 6(e) shows one prominent peak, which can be convolved into two peaks at 530.5 eV indicative of metal–oxygen bonding in line with the 530.3 eV peak in the literature, The O 1*s* peak discloses surface oxidation after exposure to air, it's percent of chemical bond is 50.45% and the data shows that CuO and Co3O4 are successfully loaded on the MWCNTs/NF electrode[21].

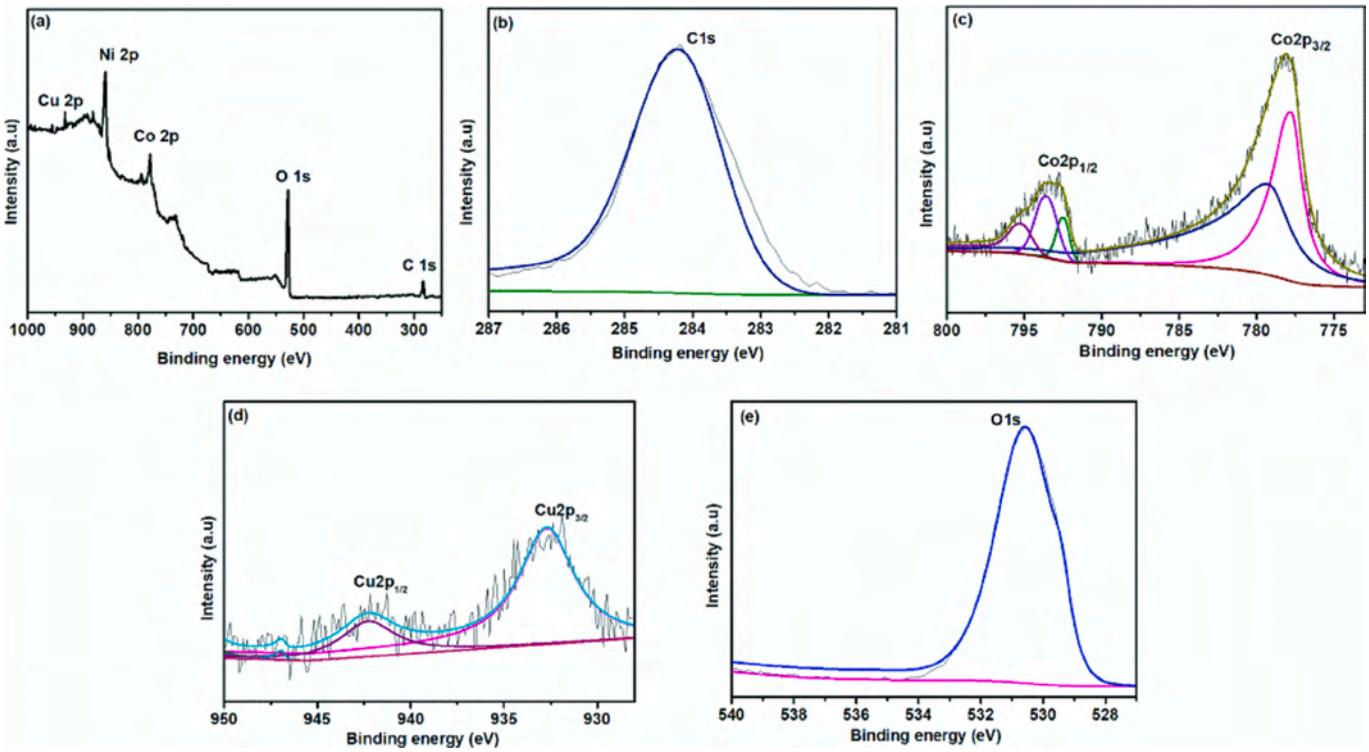

Fig. 6. XPS spectra: **(a)** Survey, **(b)** C 1*s*, **(c)** Co 2*p*, **(d)** Cu 2*p*, and **(e)** O 1*s*.

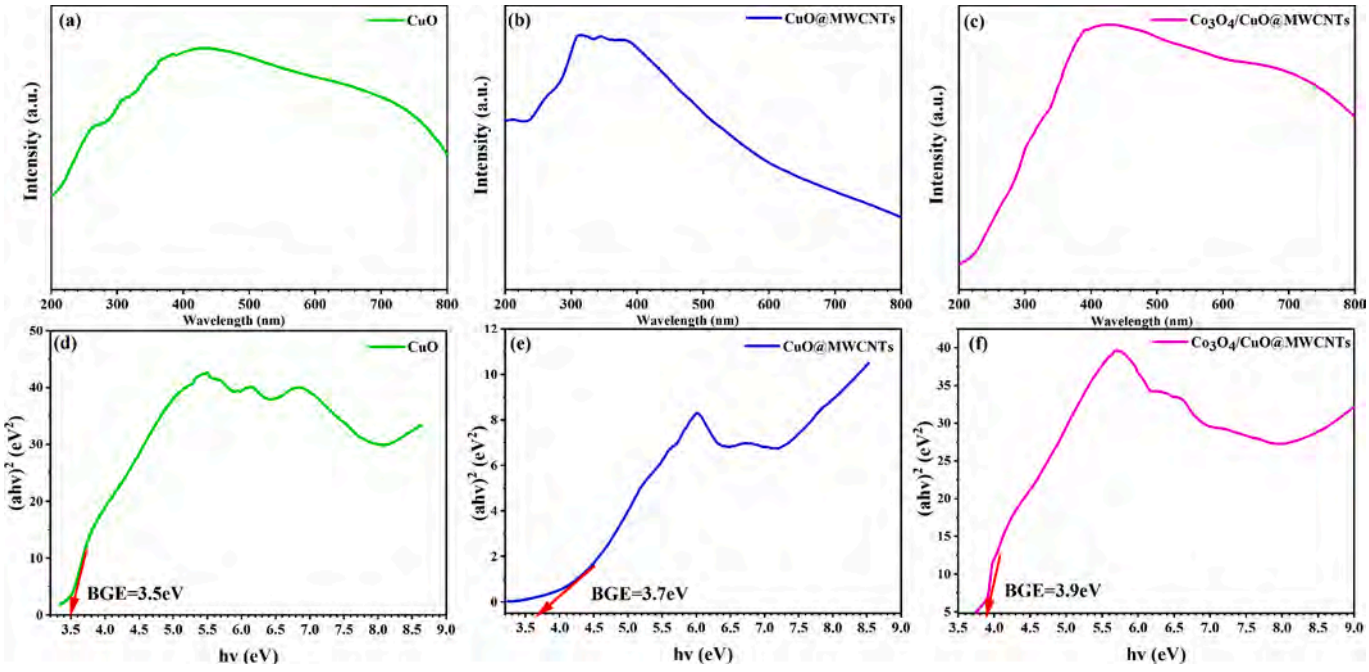

Fig. 7. UV–Visible spectra and band gap energy plot **(a.d)** CuO NPs, **(b.e)** CuO@MWCNTs NPs, and **(c.f)** Co_3O_4/CuO@MWCNTs NPs.

3.5. UV–Vis

Optical characteristic is one of the meaningful distinctiveness for the estimation of photocatalytic activity of the Co_3O_4/CuO@MWCNTs NCs. The UV–Vis diffuse reflectance (R) date for samples are displayed in Fig. 7(a-c). According to the UV–Vis spectroscopy hypothesis, the spectra and band-gap energy (BGE) of the metal oxide can be obtained as a consequence of the adsorption of radiant energy during the shifting of the external electrons of the atom to the higher energy stage. UV–Visible spectra of the CuO NPs, CuO@MWCNT NCs and Co_3O_4/CuO@MWCNTs NCs were recorded (200–800 nm) and a wide absorption bands were found in Fig. 7. Theoretical BGE of the CuO NPs (3.5 eV), CuO@MWCNT NCs (3.7 eV) and Co_3O_4/CuO@MWCNTs NCs (3.9 eV) were calculated according to the equation (6)[42,43]:

$$BGE_{(eV)} = \frac{1240}{\lambda_{max}} \tag{6}$$

3.6. Cyclic voltammetry

The electrochemical properties of the Co_3O_4/CuO@MWCNTs NCs and reference samples are determined at room temperature using a three-electrode system in which the saturated Ag/AgCl electrode, platinum electrode, and nanostructured electrode are the reference, counter and working electrodes, respectively, with 0.1 M PBS as the electrolyte in the potential window of 0–0.8 V. Fig. 8a shows that the results obtained from the bare NF and Co_3O_4/CuO@MWCNTs NCs at a scanning rate of 50 mV/s. Compared to the pristine electrode without modification (black), the electrode modified with nanomaterials (red) exhibit obvious oxidation and reduction peaks. The redox peak in the CV of the Co_3O_4/CuO@MWCNTs NCs is attributed to Co^{2+}/Co^{3+} which oxidizes L-LA to pyruvate in the solution resulting in changes in the chemical states and electron transfer boding well for enzyme-free electrochemical sensing[30,33]. The kinetics of the modified electrode is assessed at different scanning rates in order to confirm the diffusion-controlled response. Fig. 8b displays the cyclic voltammograms at different scanning rates. The CV area increase with scanning rates because of increase in the reduction and redox peaks, more active sites, and better conductivity, giving rise to accelerated diffusion. The electrochemical signal depends on the morphology of the nanocomposites. The nanostructures will an ordered morphology exhibit typical oxidation and reduction peaks as shown in Fig. 8c, which shows that the peak currents of the cathode and anode increase linearly with the square root of the scanning rates. Hence, electron transfer in Co_3O_4/CuO@MWCNTs is a diffusion-controlled electrochemical process at small scanning rates, but a surface adsorption-controlled one at large scanning rates and the results reveal that specific morphologies generate strong electrical signals.

3.7. Current-voltage characteristics

The mechanism of L-LA detection by the Co_3O_4/CuO@MWCNTs NCs is studied by obtaining the current-voltage (I-V) curves as shown in Fig. 9. L-LA is oxidized by oxygen to pyruvate and hydrogen peroxide, which then releases an electron and a proton to form an unstable intermediate. The intermediate molecule is then converted to oxygen and proton to release electrons which produce the electrochemical response from the lactate sensor[27].

In order to better detect lactic acid biomolecules, PBS is used as the electrolyte. As shown in Fig. 10(a), the current response of lactic acid molecules at different pH values (6.0, 6.5, 7.0, 7.5, and 8.0) is determined. In PBS with a pH of 8, the current observed is the largest and therefore, PBS (pH = 8.0, 0.1 M, and 50.0 mL) is selected as the electrolyte to detect lactic acid in subsequent experiments. Fig. 10(b) shows the different current response between the Co_3O_4/CuO@MWCNTs NCs and bare NF. In Fig. 10b, the blue line and the purple line represent CuO@MWCNTs NPs electrode and Co_3O_4/CuO@MWCNTs NPs electrode respectively. Their current response in the buffer can be seen that the current increases gradually after the addition of Co_3O_4 nanoparticles. It shows that the performance of Co_3O_4/CuO@MWCNTs NPs electrode is superior, which is consistent with the results in Fig. 8(a). The attachment of nanomaterials on the nickel foam electrode brings more active sites to the electrode, which makes the electrode more active and

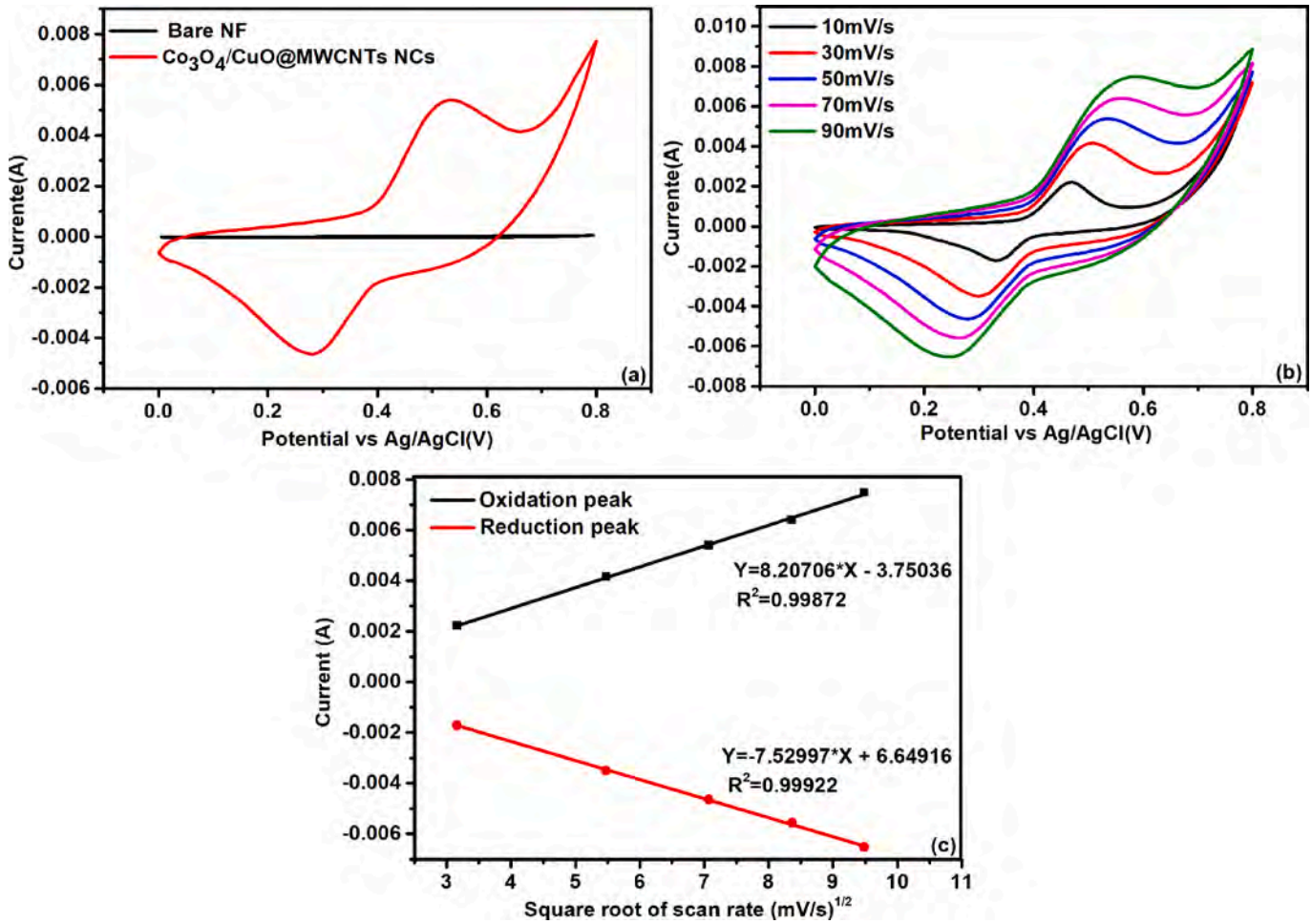

Fig. 8. (a) CV curves of the bare NF and Co_3O_4/Cuo@MWCNTs NCs electrodes at a scanning rate of 50 mV/s, **(b)** CV curves of the Co_3O_4/Cuo@MWCNTs NCs electrode at different scan rates, and **(c)** Cathodic and anodic peak currents versus square root of the scanning rates acquired from Co_3O_4/Cuo@MWCNTs NCs.

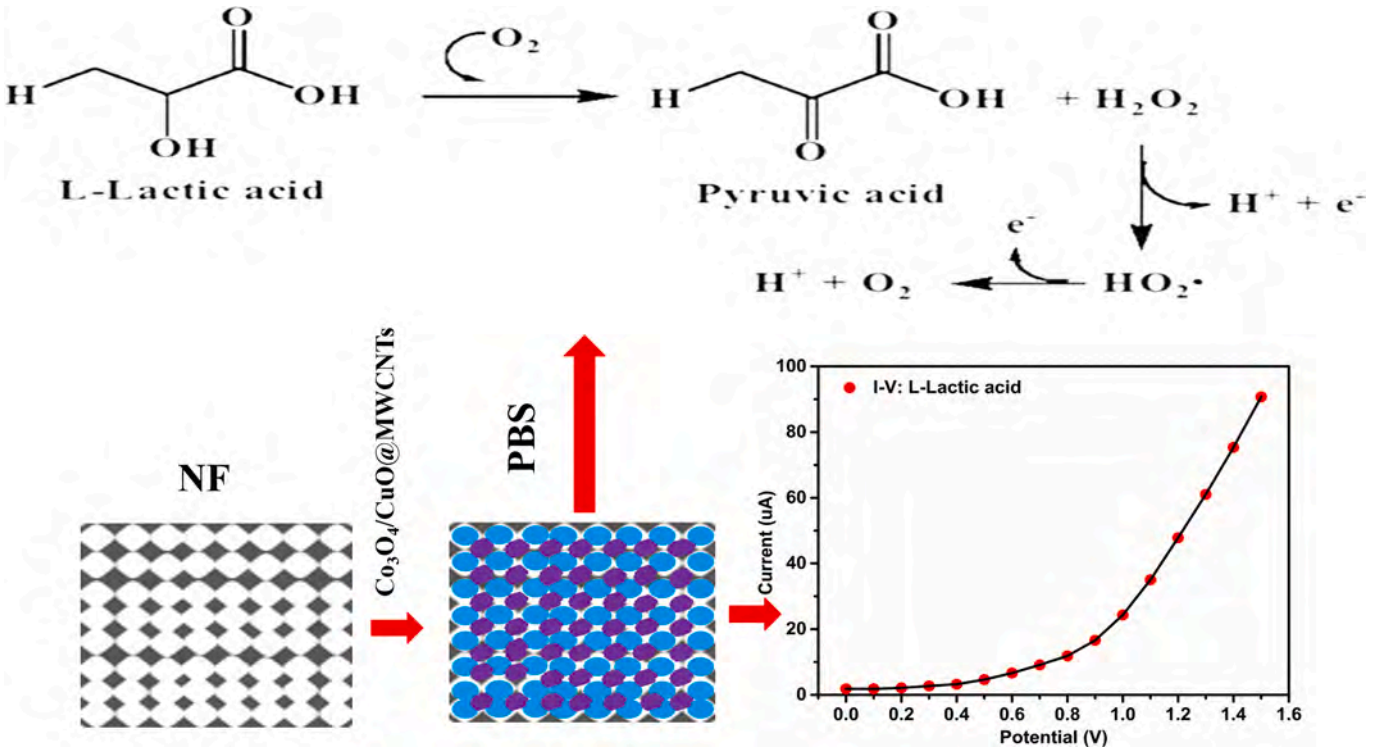

Fig. 9. Possible electrochemical mechanism for detection of L-Lactic acid by the sensor made of Co_3O_4/Cuo@MWCNTs NCs.

can obtain a larger reaction current. The red line in Fig. 8(a) corresponds to the purple line in Fig. 10(b), which further confirms that the electrode prepared by us has better electrochemical performance. The red line and blue line in Fig. 10(c) represent the current response of CuO@MWCNTs NPs electrode and Co_3O_4/CuO@MWCNTs NPs electrode in the presence of L-LA respectively. It can be seen that Co_3O_4/CuO@MWCNTs NPs electrode has a stronger current for L-LA detection than CuO@MWCNTs NPs electrode, indicating that the Co_3O_4/CuO@MWCNTs NPs electrode made by us has a higher sensitivity and Fig. 10(c) shows the current-voltage response of the modified and bare NF in the presence of 1.0 μM, 25.0 μL lactic acid in 0.1 M PBS. Co_3O_4 is a p-type semiconducting material with a direct and indirect energy bandgap of 2.10 eV and 1.60 eV, respectively. During the crystallization, it acquires Co^{3+} ions at the octahedral sites and a Co^{2+} ions at tetrahedral sites when combine with oxygen it gives a close-packed face-centered cubic structure. Due to ionic arrangement in the crystal structure, which gives different polar sites into the cobalt oxide. Moreover, Co_3O_4 has a robust an electrochemical activity. Because of the presence of cobalt, during the detection of lactic acid, a larger current response is generated through the conversion of Co^{2+}/Co^{3+}[28].

Selectivity is an important sensing parameter and in our experiments, maltose, lactose, sucrose, chitosan, oxalic acid dihydrate, uric acid, ascorbic acid, folic acid, and L-LA (1.0 μM and 25.0 μL) are introduced to PBS (pH = 8.0, 0.1 M, and 50.0 mL) to determine the selectivity. Experiments are conducted using the same modified electrode at room temperature. Due to the detection mechanism of the sensor, lactic acid oxidizes lactic acid into pyruvate in the presence of Co_3O_4/CuO@MWCNTs sensitive substances, thus releasing electrons. Due to the selectivity of the sensor, the detection current of other biomolecules will be small or no current response will be generated. The chemical reaction between the sensor and L-LA is shown as follows: $\text{L}-\text{Lactic acid} \rightarrow \text{Pyruvic acid} + H_2O_2 + e^-$ (7) The sensor is more responsive to L-LA in comparison with other molecules as shown in Fig. 10(d) thereby confirming the good selectivity[21].

The electrochemical response is evaluated based on a range of L-LA concentrations. As shown in Fig. 11(a), a potential range of 0.0 to +1.5 V is adopted. Fig. 11(b) presents the calibration curves at +0.4 V for the L-LA concentration range from 1.0 nM to 100.0 mM) and good linearity is demonstrated as shown by R^2 of 0.99327 (Standard Deviation (SD) = 0.58, n = 9). The sensitivity, Limit of detection (LOD), and Limit of quantitation (LOQ) of the Co_3O_4/CuO@MWCNTs NCs/NF sensor towards L-LA derived from the calibration plot by Equations (8–10) [21] are 31,600.0 $nA\mu M^{-1}cm^{-2}$, 55.0 pM, and 183.5 mM respectively:

$$\text{Sensitivity} = \frac{m}{A} \tag{8}$$

$$\text{LOD} = \frac{3 \times SD}{m} \tag{9}$$

$$\text{LOQ} = \frac{10 \times SD}{m} \tag{10}$$

The empirical fit is $y = 3.16 \times 10^{-5} \times + 10.02$, where the m, A, and SD represent the slope, surface area of NF, and standard deviation, corresponding to 3.16×10^{-5}, 1.0×1.0 cm^2 and 0.58, L-LA concentrations, respectively at +0.4 V. Fig. 12a shows that the response time of the Co_3O_4/CuO@MWCNTs NCs/NF for 1.0 μM and 25.0 μL L-LA is less than 5.0 s. To the best of our knowledge, the Co_3O_4/CuO@MWCNTs NCs have the lowest detection limit and highest sensitivity in the detection of lactate. Table 1 compares the results of different sensors and it is evident that the Co_3O_4/CuO@MWCNTs NCs boast the lowest detection limit and highest sensitivity [21–25]. The nonlinear I-V characteristic is considered to originate from the double Schottky barrier (DSB) formed at the grain boundary (GB). As the current-voltage characteristics are affected by transport mechanisms at the grain contact, the electrical performance can be controlled by changing the chemical surface composition and morphology of the Co_3O_4/CuO@MWCNTs particles. Compared with other methods, it is convenient and accurate that can quickly measure the residual voltage under lightning impulse and switching impulse. It has complete functions: it can not only measure the pulse peak under positive or negative

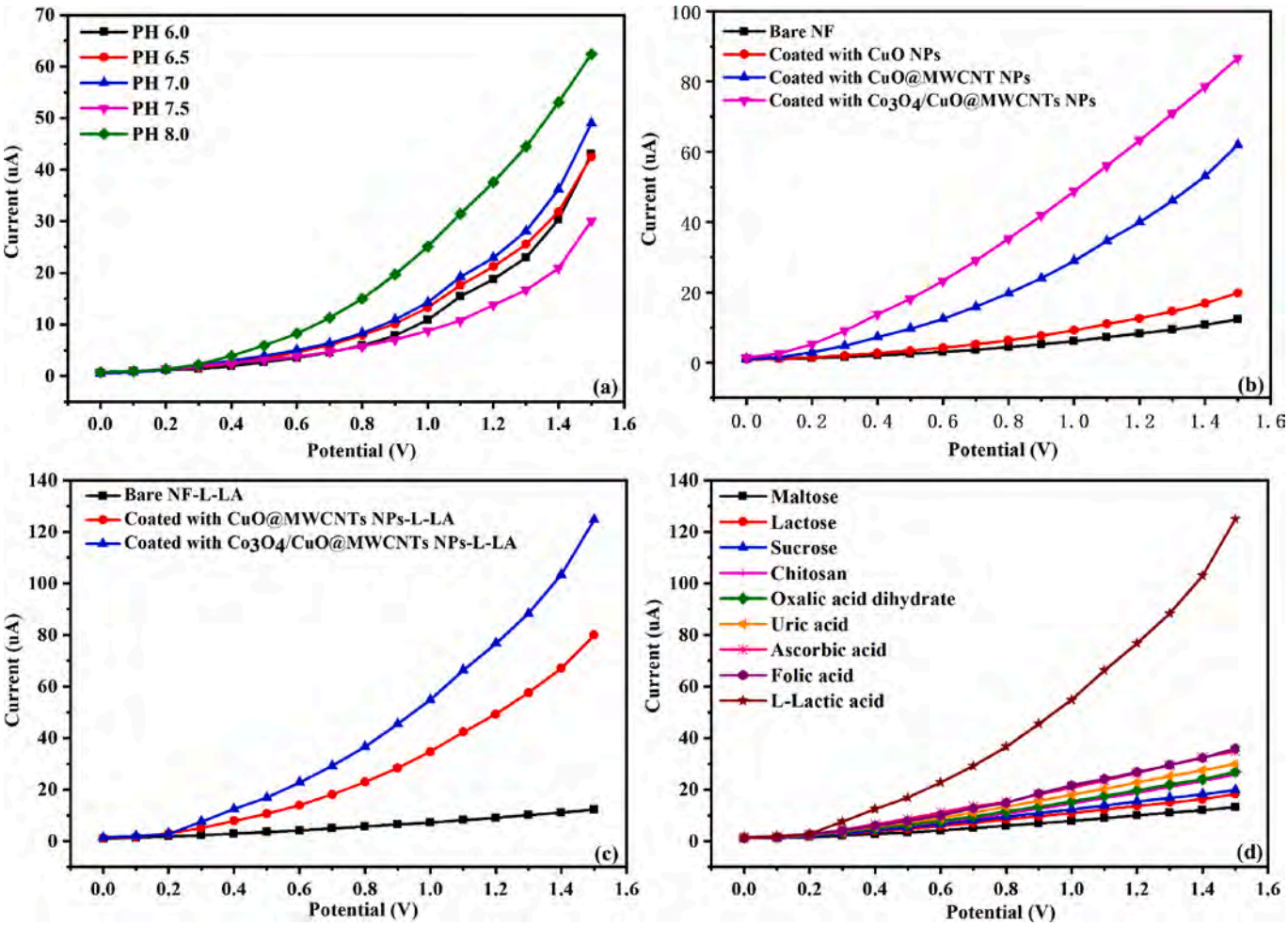

Fig. 10. **(a)** pH optimization, **(b)** Uncoated and coated CuO, CuO@MWCNTs, Co_3O_4/Cuo@MWCNTs NCs electrodes, **(c)** Presence of L-Lactic acid with uncoated and coated CuO@MWCNTs, Co_3O_4/Cuo@MWCNTs NCs electrode, and **(d)** Selectivity examination.

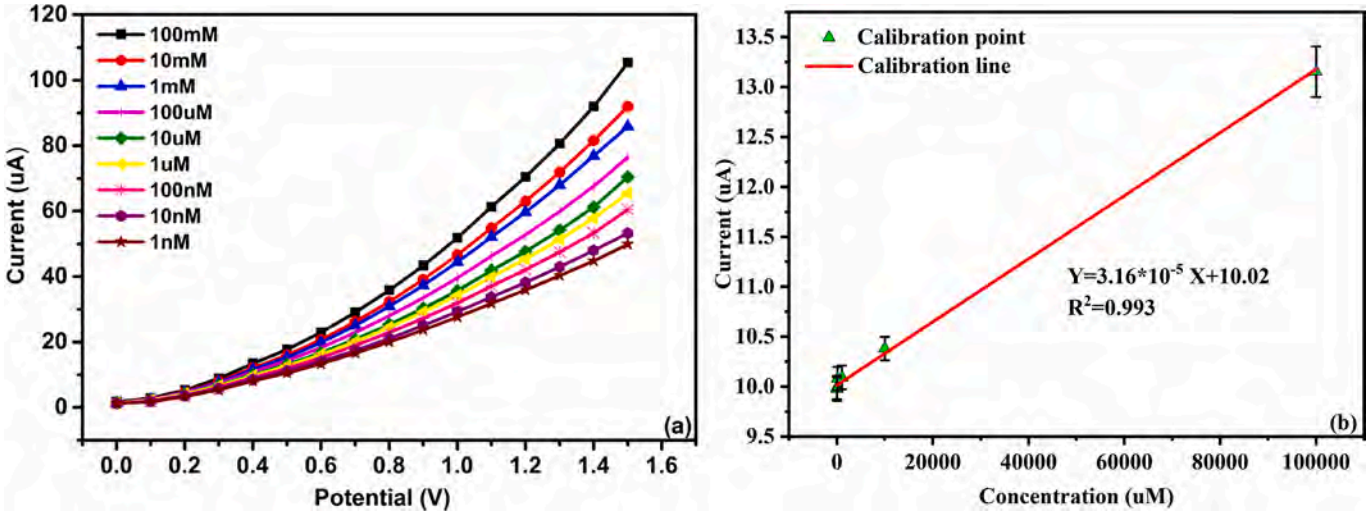

Fig. 11. **(a)** Concentration variation and **(b)** Calibration plot at +0.4 V.

polarity, but also measure the residual voltage under lightning impulse. It has the functions of current control signal indication and volt-ampere characteristic verification[48].

3.8. Analysis in sweat samples

The reproducibility and repeatability of the Co_3O_4/CuO@MWCNTs NCs/NF electrode are assessed by repeated electrocatalytic oxidation of L-LA in sweat (50 mL). A relative standard deviation (RSD) of 2.3% is

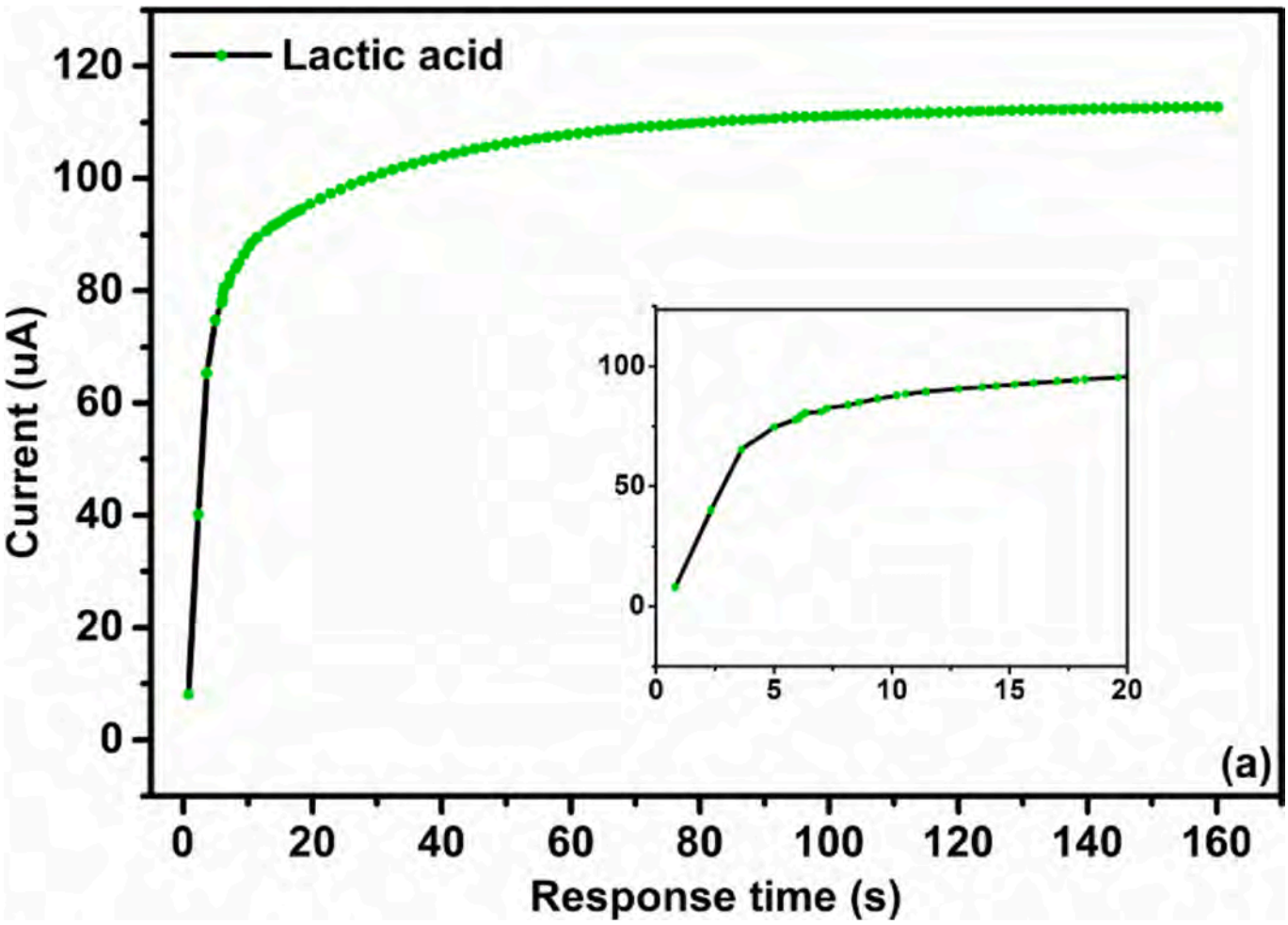

Fig. 12. Response time of L-Lactic acid on the Co_3O_4/Cuo@MWCNTs NCs/NF sensor with the inset showing the expanded plot of the response time (0–20 s).

Table 1
Comparison study of enzyme free L-Lactic acid detection using different sensors.

Working electrode	Sensitivity	Linearity	Detection limit	References
GCE/CuO.MWCNT NCs/ Nafionmatrix	633.0 $pA\mu M^{-1}cm^{-2}$	100.0 pM–10.0 mM	≈ 88.5 pM	[21]
HS-NiS/NiF	0.65 μμA $\mu M^{-1}cm^{-2}$	0.5–88.5 μM	0.023 μM	[22]
Ag NPs/NiO NPs/ PU	8.86nA mM^{-1} mm^{-2}	0.6–2.2 nM	0.38 mM	[23]
pANI/PBA-pNIPAM @CNC/CNT	—	1–25 mM	0.10 ± 0.04 mM	[24]
GCE/3-ABPA/rGO/ Au NPs	1.9×10^5 μAM^{-1}	0.1–15.0 nM	0.0089 nM	[25]
Co_3O_4/ Cuo@MWCNTs NCs	31,600 nA $\mu M^{-1}cm^{-2}$	1 nM–100 mM	55 pM	Our work

NA-not-available; GCE-glassy carbon electrode, NiO-nickel oxide, CuO-cooper oxide, pANI/PBA-polyaniline/phenylboronic acid, 3-ABPA-3-aminophenulboronic acid, NiF-nickel foam, HS-NiS-hollow sphere structured nickel sulfide, pNIPAM-poly (N-isopropylacrylamide).

calculated from three measurements showing a repeatability of 98.0% in sweat. The recovery values of the L-LA in sweat are listed in Table 2 which shows that they reach 98.3−99.3% with RSD between 0.8% and 2.3%, suggesting that the Co_3O_4/CuO@MWCNTs NCs have immense potential in clinical and biomedical analysis.

Table 2
Recovery tests of lactic acid in sweat samples (n = 3) at the Co_3O_4/Cuo@MWCNTs NCs sensing electrode.

Material	Added (μM)	Found (μM)	Recovery (%)	RSD(%)(n = 3)
Co_3O_4 /Cuo@MWCNTs NCs	0.5	0.49	98.5	0.8
	1.0	0.98	98.3	2.3
	1.5	1.49	99.3	1.7

4. Conclusion

A high-performance electrochenical sensor composed of Co_3O_4/CuO@MWCNTs NCs is prepared by a hydrothermal technique from copper sulfate pentahydrate, multi-walled carbon nanotubes, cobalt nitrate, and urea. The Co_3O_4/CuO@MWCNTs NCs have high electrocatalytic activity in oxidation of lactic acid. The CuO@MWCNTs NCs amplify the signal, the flower-like Co_3O_4 mimic the enzyme activity in oxidation of L-LA, and the CuO@MWCNTs NCs also provide excellent support to facilitate deposition of the flower-like Co_3O_4. The sensor has high sensitivity, stability, and reproducibility in spite of the presence of common interfering species such as uric acid, ascorbic acid, chitosan, folic acid, and so on. The enzyme-free sensor is simple, does not require stringent storage conditions, and can be used under ambient conditions. Furthermore, detection in sweat samples is demonstrated to confirm the practicality and the Co_3O_4/CuO@MWCNTs NCs/NF sensor has large potential in L-LA detection.

Declaration of Competing Interest

The authors declare that they have no known competing financial interests or personal relationships that could have appeared to influence the work reported in this paper.

Data availability

No data was used for the research described in the article.

Acknowledgements

We would like to thank the Engineering Research Center of Agricultural Multi-Dimensional Sensor Information Perception, Heilongjiang Province, and Heilongjiang Provincial Key Laboratory of Micro-Nano Sensor Component. This work was jointly supported by the Fundamental Research Funds in Heilongjiang Provincial Universities, Heilongjiang Higher Education Teaching Reform Project of Heilongjiang Provincial Department of Education (No SJGY20200781), Key research and development project of Heilongjiang Province (Nos. GZ20210073 and GZ20210079), Open project of Heilongjiang Key Laboratory of Micro Nano Sensors (No. WNCGQJKF202105), Fundamental Research Funds in Heilongjiang Provincial Universities (No.145109215), Heilongjiang Science Foundation Project (ZD2019F004), Shenzhen – Hong Kong Innovative Collaborative Research and Development Program (No. SGLH20181109110802117 and CityU 9240014), as well as City University of Hong Kong Strategic Research Grant (SRG) (No. 7005505).

References

[1] A.S. Meidert, B. Saugel, Evaluation of Devices for Measurement of Blood Pressure [M]. Cardiopulmonary Monitoring, Springer, Cham, 2021, pp. 273-281.
[2] M.F. Md Shakhih, A.S. Rosslan, A.M. Noor, S. Ramanathan, A.M. Lazim, A. A. Wahab, Review-Enzymatic and Non-Enzymatic Electrochemical Sensor for Lactate Detection in Human Biofluids[J], J. Electrochem. Soc. 168 (6) (2021) 067502.
[3] S. Amin, A. Tahira, A. Solangi, R. Mazzaro, Z.H. Ibupoto, A. Vomiero, A sensitive enzyme-free lactic acid sensor based on NiO nanoparticles for practical applications[J], Anal. Methods 11 (28) (2019) 3578–3583.
[4] V. Kshtriya, B. Koshti, D.K. Pandey, S. Kharbanda, C. Kanth P, D.K. Singh, D. Bhatia, N. Gour, Sequential and cellular detection of copper and lactic acid by disaggregation and reaggregation of the fluorescent panchromatic fibres of an acylthiourea based sensor[J], Soft Matter 17 (16) (2021) 4304–4316.
[5] B. Baker Lindsay, A.S. Wolfe, Physiological mechanisms determining eccrine sweat composition.[J], Eur. J. Appl. Physiol. 120 (4) (2020) 719–752.
[6] L.B. Baker, A.S. Wolfe, Physiological mechanisms determining eccrine sweat composition[J], Eur. J. Appl. Physiol. 120 (4) (2020) 719–752.
[7] P. Vaňkátová, A. Kubíčková, M. Cigl, K. Kalíková, Ultra-performance chromatographic methods for enantioseparation of liquid crystals based on lactic acid[J], J. Supercrit. Fluids 146 (2019) 217–225.
[8] L. Jiang, Y. Yang, Y. Lin, Z. Chen, C. Xing, C. Lu, H. Yang, S. Zhang, An electrochemical sensor based on enzyme-free recycling amplification for sensitive and specific detection of miRNAs from cancer cells[J], Analyst 145 (9) (2020) 3353–3358.
[9] García-Torres, Jose, Lázaro, Carmen, Sylla D, et al., Combining 2D organic and 1D inorganic nanoblocks to develop free-standing hybrid nanomembranes for conformable biosensors[J], (2022) 1-11.
[10] S. Forouzanfar, F. Alam, I. Khakpour, A.R. Baboukani, N. Pala, C. Wang, Highly sensitive lactic acid biosensors based on photoresist derived carbon[J], IEEE Sens. J. 20 (16) (2020) 8965–8972.
[11] G. Rattu, K.P. Murali, Development of non-enzymatic ZnO nanocomposite-based optical sensor for l-lactate detection in tomato samples[J], Int. J. Food Sci. Technol. 56 (9) (2021) 4328–4337.
[12] Y.-H. Nien, Z.-X. Kang, T.-Y. Su, C.-S. Ho, J.-C. Chou, C.-H. Lai, P.-Y. Kuo, T.-Y. Lai, Z.-X. Dong, Y.-Y. Chen, Y.-H. Huang, Investigation of flexible arrayed lactate biosensor based on copper doped zinc oxide films modified by iron–platinum nanoparticles[J], Polymers 13 (13) (2021) 2062.
[13] M. Arivazhagan, G. Maduraiveeran, Ultra-fine nickel sulfide nanoclusters@nickel sulfide microsphere as enzyme-free electrode materials for sensitive detection of lactic acid[J], J. Electroanal. Chem. 874 (2020) 114465.
[14] G. Maduraiveeran, A. Chen, Design of an enzyme-mimicking NiO@Au nanocomposite for the sensitive electrochemical detection of lactic acid in human serum and urine[J], Electrochim. Acta 368 (2021) 137612.
[15] K. Nishiyama, R. Mizukami, S. Kuki, A. Ishida, J. Chida, H. Kido, M. Maeki, H. Tani, M. Tokeshi, Electrochemical enzyme-based blood ATP and lactate sensor for a rapid and straightforward evaluation of illness severity[J], Biosens. Bioelectron. 198 (2022) 113832.
[16] H. Huang, D. Wang, Y. Zhou, D. Wu, X. Liao, W. Xiong, J. Du, Y. Hong, Multiwalled carbon nanotubes modified two dimensional MXene with high antifouling property for sensitive detection of ochratoxin A[J], Nanotechnology 32 (45) (2021) 455501.
[17] M.E. David, R.-M. Ion, R.M. Grigorescu, L. Iancu, A.M. Holban, A.I. Nicoara, E. Alexandrescu, R. Somoghi, M. Ganciarov, G. Vasilievici, A.I. Gheboianu, Hybrid Materials Based on Multi-Walled Carbon Nanotubes and Nanoparticles with Antimicrobial Properties[J], Nanomaterials 11 (6) (2021) 1415.
[18] A.S. Chang, N.N. Memon, S. Amin, F. Chang, U. Aftab, M.I. Abro, A. dadChandio, A.A. Shah, M.H. Ibupoto, M.A. Ansari, Z.H. Ibupoto, Facile Non-enzymatic Lactic Acid Sensor Based on Cobalt Oxide Nanostructures[J], Electroanalysis 31 (7) (2019) 1296–1303.
[19] X. Li, R. Miao, B. Tao, F. Miao, Y.u. Zang, P.K. Chu, $Co_3O_4/MnO_2/Co(OH)_2$ on Nickel Foam Composites Electrode with excellent electrochemical performance for Supercapacitor[J], Solid State Sci. 95 (2019) 105941.
[20] Z.K. Heiba, M.B. Mohamed, N.G. Imam, A.M. El-Naggar, Optical and Electrical Properties of Double-Walled Carbon Nanotube/Polyaniline Composite[J], J. Supercond. Nov. Magn. 33 (5) (2020) 1439–1445.
[21] M.M. Hussain, A.M. Asiri, M.M. Rahman, A non-enzymatic electrochemical approach for l-lactic acid sensor development based on CuO.MWCNT nanocomposites modified with a Nafion matrix[J], New J. Chem. 44 (23) (2020) 9775–9787.
[22] F. Miao, X. Li, B. Tao, P.K. Chu, Heterostructured $Co(OH)_2$ nanosheet-coated $CuCo_2S_4$ nanopencils on nickel foam for electrodes in high-performance supercapacitors[J], Ionics 26 (10) (2020) 5241–5249.
[23] Y.-S. Huang, K.-Y. Chen, Y.-T. Cheng, C.-K. Lee, H.-E. Tsai, An inkjet-printed flexible non-enzymatic lactate sensor for clinical blood plasma test[J], IEEE Electron Device Lett. 41 (4) (2020) 597–600.
[24] S.M. Mugo, Dhanjai, J. Alberkant, A Biomimetric Lactate Imprinted Smart Polymers as Capacitive Sweat Sensors[J], IEEE Sens. J. 20 (11) (2020) 5741–5749.
[25] M. Arivazhagan, A. Shankar, G. Maduraiveeran, Hollow sphere nickel sulfide nanostructures-based enzyme mimic electrochemical sensor platform for lactic acid in human urine[J], Microchim. Acta 187 (8) (2020) 1–9.
[27] C. Zhang, T. Wang, Y. Ding, Oxidative dehydrogenation of lactic acid to pyruvic acid over Pb-Pt bimetallic supported on carbon materials[J], Appl. Catal. A 533 (2017) 59–65.
[28] W.L. Roth, The magnetic structure of Co_3O_4[J], J. Phys. Chem. Solid 25 (1) (1964) 1–10.
[29] R. Santhosh Kumar, K. Govindan, S. Ramakrishnan, A.R. Kim, J.-S. Kim, D.J. Yoo, Fe_3O_4 nanorods decorated on polypyrrole/reduced graphene oxide for electrochemical detection of dopamine and photocatalytic degradation of acetaminophen[J], Appl. Surf. Sci. 556 (2021) 149765.
[30] C. Karthikeyan, K. Ramachandran, S. Sheet, et al., ACS Sustainable Chem[J], Eng 5 (2017) 4897–4905.
[31] K. Ramachandran, K. Babu, G.G. Kumar, et al., One-pot synthesis of graphene supported CuO nanorods for the electrochemical hydrazine sensor applications[J], Sci. Adv. Mater. 7 (2) (2015) 329–336.
[32] P. Vennila, D.J. Yoo, A.R. Kim, Ni-Co/Fe_3O_4 flower-like nanocomposite for the highly sensitive and selective enzyme free glucose sensor applications[J], J. Alloy. Compd. 703 (2017) 633–642.
[33] R. Elamathi, R. Ramesh, M. Aravinthraj, et al., Investigation of structural and electrical properties of lithium cobalt oxide nanoparticles for optoelectronic applications[J], Surf. Interfaces 20 (2020), 100582.
[34] S.S. Rathnakumar, K. Noluthando, A.J. Kulandaiswamy, et al., Stalling behaviour of chloride ions: a non-enzymatic electrochemical detection of α-Endosulfan using CuO interface[J], Sens. Actuators B 293 (2019) 100–106.
[35] A.M. Amanulla, S.K.J. Shahina, R. Sundaram, et al., Antibacterial, magnetic, optical and humidity sensor studies of β-CoMoO4-Co_3O_4 nanocomposites and its synthesis and characterization[J], J. Photochem. Photobiol. B Biol. 183 (2018) 233–241.
[36] J. Kennedy, F. Fang, J. Futter, et al., Synthesis and enhanced field emission of zinc oxide incorporated carbon nanotubes[J], Diam. Relat. Mater. 71 (2017) 79–84.
[37] Z.K. Heiba, L. Arda, N. Dogan, et al., The investigation of structural and magnetic properties of $Er_2-xCoxO_3$ nano-oxides[J], J. Mater. Sci. Mater. Electron. 33 (1) (2022) 1–10.
[38] Z.K. Heiba, M.B. Mohamed, A. Abd Ellatief, et al., Influence of composition ratio on structural, optical and magnetic properties of $NiFe_2O_4/(1x)MnOxCoO$ composites [J], J. Mater. Sci. Mater. Electron. 33 (30) (2022) 23555–23565.
[39] Z.K. Heiba, M.B. Mohamed, A. Badawi, Structural and Optical Characteristic of Cu-Doped TiO_2 Thin Film[J], J. Inorg. Organomet. Polym Mater. (2022) 1–10.
[40] Z.K. Heiba, M.B. Mohamed, A. Ellatief, et al., Structural, optical, and magnetic properties of ferrite/oxide composites $MgFe_2O_4/(1–x)$ MnO-xCdO[J], Appl. Phys. A 128 (10) (2022) 1–12.
[41] Z.K. Heiba, M.B. Mohamed, M. Abdellatief, et al., Optical and Magnetic Studies of Y-Doped Nano γ-Fe_2O_3[J], J. Inorg. Organomet. Polym Mater. 32 (10) (2022) 3826–3836.

[42] Z.K. Heiba, M.B. Mohamed, A. Abd Ellatief, et al., Influence of composition ratio on structural, optical and magnetic properties of $NiFe_2O_4$/(1–x) MnO−xCoO composites[J], J. Mater. Sci. Mater. Electron. (2022) 1–11.
[43] Z.K. Heiba, M.B. Mohamed, A.A. Alkathiri, et al., Impact of composition ratio on the structure and optical properties of (1–x) $MnFe_2O_4$/(x) $ZnMn_2O_4$ nanocomposite [J], Chin. Phys. B (2022).
[44] G. Qi, Y. Liu, L. Chen, et al., Lightweight Fe_3C@ Fe/C nanocomposites derived from wasted cornstalks with high-efficiency microwave absorption and ultrathin thickness[J], Advanced Composites and Hybrid Materials 4 (4) (2021) 1226–1238.
[45] Z. Zhang, M. Liu, M.M. Ibrahim, et al., Flexible polystyrene/graphene composites with epsilon-near-zero properties[J], Adv. Compos. Hybrid Mater. (2022) 1–13.
[46] P. Xie, Z. Shi, M. Feng, et al., Recent advances in radio-frequency negative dielectric metamaterials by designing heterogeneous composites[J], Adv. Compos. Hybrid Mater. (2022) 1–17.
[47] H. Wu, Y. Zhong, Y. Tang, et al., Precise regulation of weakly negative permittivity in $CaCu_3Ti_4O_{12}$ metacomposites by synergistic effects of carbon nanotubes and grapheme[J], Adv. Compos. Hybrid Mater. 5 (1) (2022) 419–430.
[48] I. Pleșa, S. Radl, U. Schichler, et al., Influence of morphology and chemical surface composition on electrical conductivity of SiC microspheres[J], Surf. Sci. 715 (2022), 121942.
[49] S. Mercan, A comprehensive artificial sweat study for quantitation of nickel and other inorganic elements released from imitation earrings purchased in Istanbul market[J], Biol. Trace Elem. Res. 194 (1) (2020) 303–312.

Further reading

[26] K. Du, F. Ernst, Quantitative assessment of nanoparticle size distributions from HRTEM images[J], Int. J. Mater. Res. 97 (7) (2022) 928–933.